# Unraveling the dealloying mechanism of a Au33Fe67 metastable precursor for a low-cost nanoporous gold production

*Original Citation:*

*Availability:*

This version is available http://hdl.handle.net/2318/2056911 since 2025-02-14T11:18:08Z

*Published version:*

DOI:10.1016/j.jallcom.2024.175984

# Unraveling the dealloying mechanism of a $Au_{33}Fe_{67}$ metastable precursor for a low-cost nanoporous gold production

Journal of Alloys and Compounds 1005 (2024) 175984

Deepti Raj [a], Gianluca Fiore [a], Federica Celegato [b], Marco Coïsson [b], Gabriele Barrera [b,*], Federico Scaglione [a,*], Paola Tiberto [b,1], Paola Rizzi [a,1]

[a] *Dipartimento di Chimica e Centro Interdipartimentale NIS (Nanostructured Surfaces and Interfaces), Universita` di Torino, Via Pietro Giuria 7, Torino 10125, Italy*
[b] *Istituto Nazionale di Ricerca Metrologica (INRIM), Str. delle Cacce 91, Torino 10135, Italy*

* Corresponding authors.
*E-mail addresses:* g.barrera@inrim.it (G. Barrera), federico.scaglione@unito.it (F. Scaglione).
[1] co-last author: P. Rizzi and P. Tiberto

https://doi.org/10.1016/j.jallcom.2024.175984

# Unraveling the dealloying mechanism of a $Au_{33}Fe_{67}$ metastable precursor for a low-cost nanoporous gold production

Deepti Raj [a], Gianluca Fiore [a], Federica Celegato [b], Marco Coïsson [b], Gabriele Barrera [b,*],
Federico Scaglione [a,*], Paola Tiberto [b,1], Paola Rizzi [a,1]

[a] *Dipartimento di Chimica e Centro Interdipartimentale NIS (Nanostructured Surfaces and Interfaces), Universita` di Torino, Via Pietro Giuria 7, Torino 10125, Italy*
[b] *Istituto Nazionale di Ricerca Metrologica (INRIM), Str. delle Cacce 91, Torino 10135, Italy*

## Abstract

A low-cost Nanoporous Gold (NPG) has been successfully prepared by chemical dealloying of a $Au_{33}Fe_{67}$ supersaturated solid solution, whose ribbons were obtained by rapid solidification using melt-spinning technique. The dealloying procedures were carried out in 1 M $HNO_3$ at 70 C for varying durations. As-quenched ribbon and dealloyed samples have been structurally and compositionally investigated using XRD, FESEM and EDS techniques. The obtained NPG is homogeneous with tunable ligament size and shape, easy-to-handle and free- standing. Most notably, a metastable precursor has been favourably obtained from an immiscible Au-Fe system. Furthermore, according to the characterization results, a mechanism of dealloying has been proposed. Pairing Au with cheap and abundant Fe and fabricating an Fe-rich precursor gives an exceedingly cost-effective starting material. No usage of critical raw materials is involved. Then, employing a straight-forward and rapid dealloying procedure to obtain the NPG sample, makes for an overall inexpensive and sustainable production.

**Keywords:** Nanoporous Gold, Au-Fe, Dealloying Mechanism, Magnetic properties

## 1. Introduction

There has been plenty of emergent interest in Nanoporous gold (NPG) credited to its intriguing properties and numerous applications from chemical sensing, electrochemical and optical bio-sensing to catalysis, mechanical actuation and many more [1–7]. NPG is built in the form of a 3-dimensional network of interconnected ligaments and pores with adaptable size and shape that affect the resultant chemical and physical properties. This scope of tunability and flexibility provides the opportunity of influencing the properties according to the targeted application. Additionally, NPG has a high surface area-to-volume ratio and is fairly easy to prepare and handle, which all work to its advantage. Dealloying is a popular technique for the preparation of NPG which is known as the selective removal of a less noble metal from a solid solution alloy [8]. The process of dealloying is usually accompanied by surface diffusion, the ad-atoms of the remnant more noble metal reorganize and rearrange into interconnected ligaments simultaneously creating pores [9–11]. For a successful process of dealloying it is vital to obey the parting limit while choosing the composition of the precursor alloy that is defined as the minimum concentration of the more noble component in the alloy above which dealloying cannot occur [8,12,13]. The precursor alloy is then placed in a suitable electrolyte for a defined period at a specific temperature. This etching electrolyte needs to be carefully chosen by interpreting Pourbaix diagrams for electrochemical techniques such that it selectively eliminates the less noble metal. Altering the experimental conditions, i.e., concentration, pH and type of electrolyte, temperature and time of dealloying can result in uniquely different NPG properties. This remarkable aspect of the dealloying method provides the room for designing, tuning and producing particular microstructures and morphologies [3,6,14].

The Au-Fe system has been the subject of interesting studies in the recent past and as a precursor for NPG it holds a particular interest. From the phase diagram a strikingly huge miscibility gap can be observed between the metals in their solid state [14,15]. The metals can be forced to form a metastable supersaturated solid solution by rapid solidification [16,17]. However, studies on the production of NPG from this unique system via dealloying are numbered. Differently from our previous works [18] where we have dealt with the application of this NPG as a substrate for SERS and as electrocatalyst for the hydrogen evolution reaction, this paper presents a detailed study of the fabrication and characterization of NPG from a biphasic metastable supersaturated solid solution of Au-Fe with an Fe-rich composition thereby throwing light on the underlying dealloying mechanism. The precursor is composed of 33 at% Au and 67 at% Fe, respecting the parting limit of Au, which was subjected to chemical dealloying in 1 M HNO3 at 70 ◦C for durations ranging from 1 minute to 8 hours. The samples have been characterized by advanced techniques to investigate their structural, morphological and magnetic properties and results obtained are key points to achieve a specific control of the design of NPG with peculiar properties. Furthermore, another important objective of this work has been to synthesize high quality NPG in a low-cost and sustainable manner. The goal of a cost-effective NPG was achieved by pairing Fe, an inexpensive [19] and abundant metals with Au that is expensive but added in the precursor in its lowest possible amount, in accordance with the parting limit. Avoiding the use of any critical raw material [20] and selecting a diluted aqueous electrolyte of nitric acid, that is one of the most common and price affordable chemicals, we made the overall procedure as sustainable.

## 2. Experimental

Au$_{33}$Fe$_{67}$ master alloy of target composition 33 at% Au and 67 at% Fe was prepared from pure elements (99.99 % Au and 99.95 % Fe) by arc- melting in Ti-gettered Ar atmosphere. Several remelting cycles were performed to ensure homogeneity. Subsequently, melt-spinning technique was utilized to rapidly quench the obtained ingot and produce thin, long ribbons 40 μm thick and 8 mm wide [21]. Quartz crucible of 2 mm nozzle size was used through which the molten ingot was ejected onto a cold and hardened Cu wheel (1.5 mm distance to wheel) rotating at a 25 m s$^{-1}$ linear speed in a closed chamber kept under Ar atmosphere (1 bar chamber pressure, +0.2 bar overpressure).

The as-quenched Au$_{33}$Fe$_{67}$ ribbon was subjected to chemical dealloying in 1 M HNO$_3$ at 70 ◦C for different lengths of time ranging from 1 min to 8 h. A thickness of 20–25 μm was measured for samples after long dealloying time. After dealloying, the sample retains its free- standing and mechanical stability, making it easy to handle for various applications. Chemical grade reagents and deionized water were used for the preparation of the required electrolytes. As-prepared samples were rinsed in deionized water and dried before characterization.

Compositional and structural investigation of the master alloy, as- quenched ribbon, and as-dealloyed samples, was enabled by using a PANalytical X'pert X-ray diffractometer in Bragg–Brentano geometry with monochromatic Cu K radiation, scanning electron microscopy (Inspect SEM, FEI), field-emission scanning electron microscopy (FIB- FE-SEM/EBSD/EDS/TOF-SIMS Tescan S9000G microscope), and connected to energy dispersive X-ray spectroscopy (Oxford Ultim-Max 100 FE- SEM). Metallography studies of the nanoporous samples were conducted using ImageJ an open source software for processing and analysing scientific images; in detail, the average ligament size and its standard deviation was measured at the narrower neck of the ligaments by ana- lysing 100 ligaments per sample [22–24]. Rietveld analyses of XRD patterns was conducted with Maud soft- ware [25] using the size/microstrain anisotropic Popa model for the fitting of reflections. The refining was conducted by modelling the pattern with the four phases that appear in the patterns: two are fcc (Au) solid solutions, respectively named fcc (Au) and fcc (Au)#2, which differ from each other in the amount of iron in solid solution; a bcc α (Fe) solid solution; and fcc pure Au constituted by almost pure gold. The evolution of the pristine phases during dealloying has been studied by evaluating the weight percentage of each phase and their lattice parameter as a function of the dealloying time. Magnetic characterization was performed by a highly sensitive alternating field magnetometer (AGFM, Princeton Measurements Cor- poration) operating in the magnetic field range ± 18 kOe. The magnetic field was applied along both the out-of-plane and in-plane direction of the samples. The magnetic parameters such as coercive field (Hc) and saturation magnetization (Ms) were directly evaluated from the M(H) curves.

## 3 Results and discussion

### 3.1 Microstructures of the precursor obtained from rapid solidification

The $Au_{33}Fe_{67}$ alloy, which composition was confirmed by EDS, was produced by rapid solidification by melt spinning. This process induces different solidification rates depending on the side of the ribbon, i.e., the melt that is in contact with the wheel (wheel side) experiences faster cooling rates with respect to the opposite side (air side). This, in turn, produces a variable microstructure with finer crystalline grains on the wheel side and coarser microstructure on the air side. From the Au-Fe phase diagram, it can be observed that at room temperature there is no miscibility between fcc Au and bcc Fe, while increasing the temperature, solid solutions are formed. When a rapid solidification is performed, supersaturated solid solution is expected at room temperature. As can be observed in the SEM images reported in Fig. 1, two phases are visible: bcc α(Fe) (dark phase) and fcc (Au) (white phase) on both sides of the ribbon. The microstructure is finer on the wheel side, as expected, due to higher solidification rates.

The microstructure of the as-quenched ribbon has been analysed in detail in a previously published paper from our research group and from a former structural analyses no significant preferred orientation has been observed, confirming the phases described in the microstructure of the ribbons [18]. Despite no significant structural differences from the air and the wheel side of ribbons, for the sake of clarity, all the structural and microstructural characterization in this work have been conducted on the wheel side of ribbons that experiences the fastest cooling rate.

In Fig. 2(a), XRD pattern of the as-quenched ribbon reveals the peaks representing the metastable supersaturated solid solutions fcc (Au) and bcc α(Fe), marked with orange dash-dots and blue dash lines respectively. Peak assignment has been performed according to the ICDD Au reference pattern 03–065–8601 (pink dash) and Fe reference pattern 03–065–4899 (light green dash). It is worth observing that the peaks representing the fcc (Au) phases have shifted towards higher angles away from the typical diffraction angles of pure Au [26]. This is because of accommodation of Fe atoms in the Au crystalline structure leading to a decrease in the fcc (Au) lattice parameter. A similar observation can be made for the peaks of bcc α(Fe) that are shifted to lower diffraction angles as a result of incorporation of Au atoms in solid solution with Fe giving an incremented lattice parameter. The calculated lattice parameters of (Fe) and (Au) phases in the as-quenched ribbon (0.294 nm, 0.399 nm respectively) support the shifting of the peaks.

It is noteworthy that (Au) peaks have a high full width at half maximum (FWHM) that can be related both to the small size of the crystalline grains and to the presence of a gradient in composition of the supersaturated solid solution. As the solidification rate is fast and Au and Fe are thermodynamically immiscible at room temperature, it can be expected that a higher amount of Fe remains entrapped in solid solution with Au during cooling when a higher quenching rate is used, while the system will be prone to go toward the thermodynamic stability when lower cooling rates are experienced.

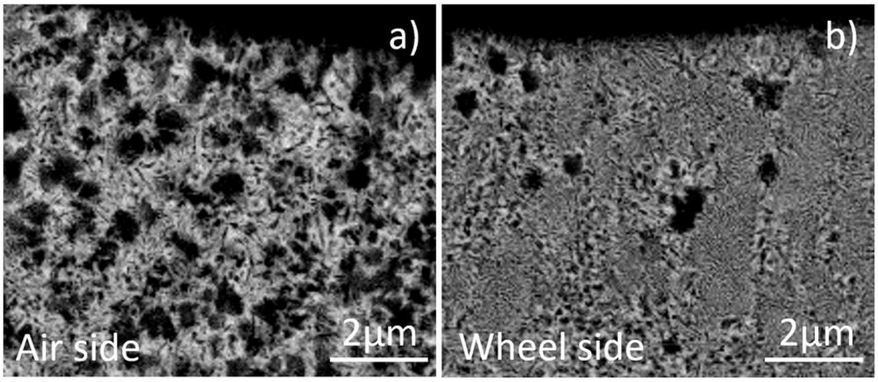

**Fig. 1.** Cross-section view of the as-quenched in BSE (Back Scattered Electron). The differences on the air side (a) and wheel side microstructure (b) are evidenced.

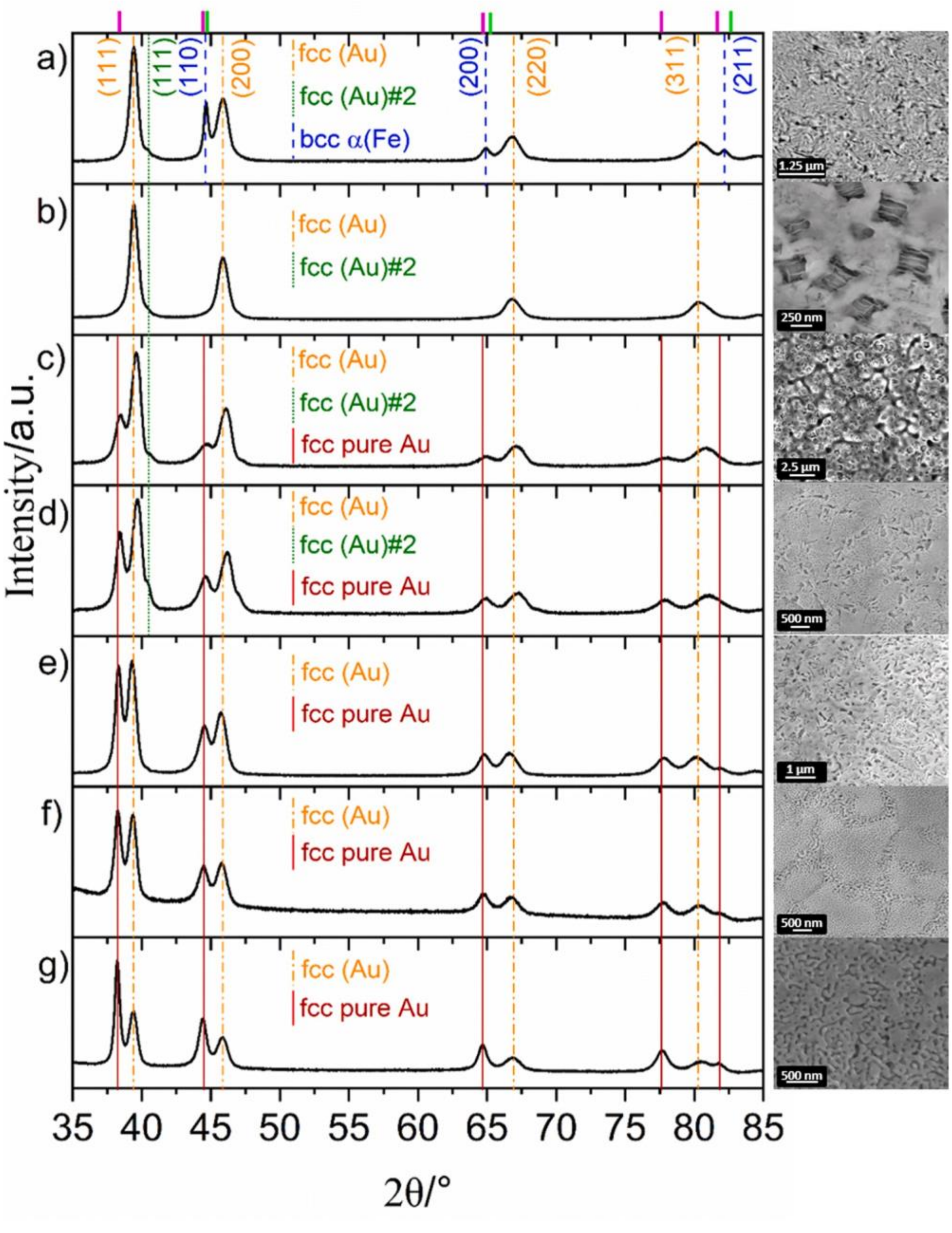

**Fig. 2.** XRD patterns of (a) the as-quenched ribbon, (b) NPG_1min (c) NPG_5min, (d) NPG_10min, (e) NPG_30min, (f) NPG_1h and (g) NPG_8h. Pink dash is Au reference pattern 03–065–8601 and light green dash is Fe reference pattern 03–065–4899. Attached to each XRD pattern is the respective sample's SEM image.

This means that a gradient in composition of the supersaturated fcc (Au) solid solution can be expected from wheel to air side, with higher Fe solute content on the surface in direct contact with the quenching medium (i.e. the copper wheel) and gradually decreasing going toward the air side. This effect is observed in the XRD pattern that presents peaks with high full width at half maximum. Moreover, a low intensity shoulder can be observed to the right of the (111) peak of (Au) phase. This also has to be interpreted as an indicator of low amount of a supersaturated fcc (Au) solid solution with a slightly different lattice parameter (0.388 nm) due to a difference in the amount of Fe solute in the lattice and it has been named fcc (Au) #2. Owing to the very limited amount of this phase that completely disappears after 30 minutes of dealloying, and due to the fact that it has the same behaviour as the fcc (Au), it will be included, in the rest of the work, in the description of the fcc (Au).

### 3.2 Chemical dealloying

Nitric acid was used as the dealloying electrolyte considering the fact that it is a strong and efficient electrolyte to easily and selectively remove Fe from the alloy matrix, while Au remains immune to the etching action of $HNO_3$. The as-quenched ribbon underwent chemical dealloying in 1 M $HNO_3$ at 70 °C for 1 min, 5 min, 10 min, 30 min, 1 h, 2 h, 4 h, 6 h and 8 h; the resulting samples were respectively named as NPG_1min, NPG_5min, NPG_10min, NPG_30min, NPG_1h, NPG_2h, NPG_4h, NPG_6h and NPG_8h.

XRD pattern for NPG_1min in Fig. 2(b) conveys the presence of the gold rich fcc(Au) phases while, at this stage, XRD pattern is devoid of peaks of bcc α(Fe) phase. The corresponding SEM image, on the right, displays that the dendrites originally present on the air side are partially empty, confirming the only presence of remnant fcc (Au) lamellae that were alternated in the as-quenched ribbon with the bcc α(Fe) phase. It means that the less noble phase in the sample, i.e., the iron rich bcc α(Fe) phase, has been eliminated as a result of a galvanic effect in play during the first minute of dealloying, from the surface of the sample and from the inner part reachable by the electrolyte due to percolation in the spaces left empty by the removed bcc α(Fe) grains.

When the time of dealloying is increased to 5 min, for NPG_5min we can observe in Fig. 2(c) the emerging peaks of a new fcc phase (marked by a full garnet line) with lattice parameter and structure close to that of pure Au. It denotes that a proper dealloying mechanism is in action causing removal of Fe atoms from the fcc (Au) solid solution that starts after the dissolution of the reachable bcc α(Fe) phase into the electrolyte. The accompanying surface diffusion leads Au adatoms to migrate and self-assemble on the surface of the pristine fcc (Au) phase resulting in formation of Au-rich ligaments. The peaks of the pristine fcc (Au) phase are also clearly visible in the pattern, not being fully dealloyed after the short duration of dealloying (Fig. 2(d)). The lower peak intensities of the new fcc phase (i.e., fcc pure Au) compared to those of the pristine fcc (Au) phase indicate that the dealloying process has impacted only a small volume of precursor at this stage, generating a limited number of ligaments. It is worth noting that by XRD, just the surface of the sample can be investigated, so the presence of remaining bcc α(Fe) phase in the bulk of the ribbon cannot be evidenced. We can expect that part of this phase remains surrounded by fcc (Au) phase and therefore, not in contact with the electrolyte.

Afterwards, as a function of the dealloying time, the fcc pure Au peaks intensity increases while the intensity of the fcc (Au) peaks decreases as shown in Fig. 2(e) to (g). Fig. 3 reports SEM images of the top surface of NPG_5min in SE on the left (a, c) and BSE on the right (b, d). As expected from the XRD pattern, it can be observed that the process of dealloying has been initiated. Fine ligaments can be located throughout the surface forming small networks within adjacent regions. The morphology seems rough at this stage with interconnected yet slightly separated regions. The remnant Au lamellae, initially interconnected to the bcc α(Fe) phase in the as-quenched sample, are also merging with their neighbouring ligaments.

Similarly, for NPG_10min and NPG_30min the intensity of the pure Au phase gradually enhances with the dealloying time at the expense of the pristine fcc (Au) phase, implying further elimination of Fe leading to a surge in the number of ligaments being formed, evidenced by the XRD patterns in Fig. 2(d) and (e) respectively. From the corresponding SEM image of NPG_10min, it seems that the continuing dealloying process and gradual ligament formation is producing areas of small ligaments while the rest of the surface, i.e., the pristine fcc (Au) phase, remains comparatively compact. These zones of ligaments are certainly originating from the coalescence of the fcc Au lamellae with ligaments in the vicinity as a result of diffusion of nearby Au atoms on the surface of the pristine phases. The compact areas seem to require more dealloying time to overcome passivation and form ligaments. As for NPG_30min, the surface cannot be differentiated based on morphologies as was in the case of NPG_10min. Further dealloying treatment seems to overcome the compactness of the surface and enable formation and merging of ligaments. When it comes to NPG_1h, the intensity of the pure Au peaks overcome that of the fcc (Au) pristine phase, visible in Fig. 2(f). The estimated lattice parameter value of 0.396 nm endorses the existence of the Au-rich fcc (Au) pristine phase. Underneath the pure Au-rich layer produced by Au ad-atoms via surface diffusion, the pristine phase resides in the ligament core being almost unsusceptible to the dealloying action as deduced from the slight change in the amount of Fe in the fcc (Au) phase, proved by a slight change in the lattice parameter of the fcc (Au) phase calculated with Rietveld analysis. The surface achieves a wide-spread dual morphology: zones of fine ligaments (29 nm approximately) bounded by relatively thicker ligaments (52 nm approximately). The pristine fcc (Au) phase experiences slower dealloying rate due to passivation offered by the high Au content with surface-diffusion mediated coarsening which yields thicker ligaments. As discussed earlier, due to a gradient in quenching rate, Au and Fe content has been variedly distributed in the as-quenched ribbon which influenced the kinetics of dealloying and that clearly instigated the bimodal morphology. For NPG_8h, the XRD pattern in Fig. 2(g) depicts further enhancement in the peak intensities for pure Au indicating generation of more Au-rich ligaments from the pristine phase, whose peaks are conversely diminished in intensity, credited to the prolonged dealloying action. However, this longer treatment has not entirely dealloyed the pristine phase with an amount of Fe still prevailing in the solid solution phase. The SEM-SE images of top surface of NPG_2h, NPG_4h, NPG_6h and NPG_8h, in Fig. 4, reveal that the morphological distinction seen in NPG_1h has begun to vanish and the overall morphology continues to progressively acquire homogeneity by fusion of nearby ligaments with extended dealloying time. At the same time slight coarsening is also evident that, consequentially, leads to coverage of some nanopores as seen in NPG_8h.

The cross sections of the NPG samples from 1 min of dealloying to1 h and 8 h are presented in Fig. 5 which can be seen as acquiring a homogeneous nanoporous morphology slowly and progressively, starting from the rough morphology of NPG_1min (Fig. 5(a)) to the most homogenous and widespread in NPG_8h (Fig. 5(f)). The EDS analysis gives the Au and Fe composition of each sample as follows: 61 at% Au and 39 at% Fe for NPG_1min; 62 at% Au 38 at% Fe for NPG_5min; 43 at% Au and 57 at% Fe for NPG_10min, 74 at% Au and 26 at% Fe NPG_30min, 65 at% Au and 35 at% Fe for NPG_1h; 71 at% Au and 29 at% Fe for NPG_2h; 81 at% Au and 19 at% Fe for NPG_4h; 88 at% Au and 12 at% Fe for NPG_6h; and 92 at% Au and 8 at% Fe for NPG_8h. Compositional analyses of ligaments is reported in Fig. 6 for all samples from 1 to 8 hours of dealloying; shorter durations of dealloying were not reported since the fluctuation of composition might be attributed to the smaller size of ligaments compared to the beam spot, thus the values reflect an average of the alloy composition instead of the composition of ligaments itself. The EDS analyses conducted in the cross section is in agreement with the previous results and thus, it does not show a gradient of composition from the surface to the inner part of the ribbon. Moreover, in the same figure the ligament size increases as a function of dealloying time and it seems to stabilize around 50 nm after 6 hours.

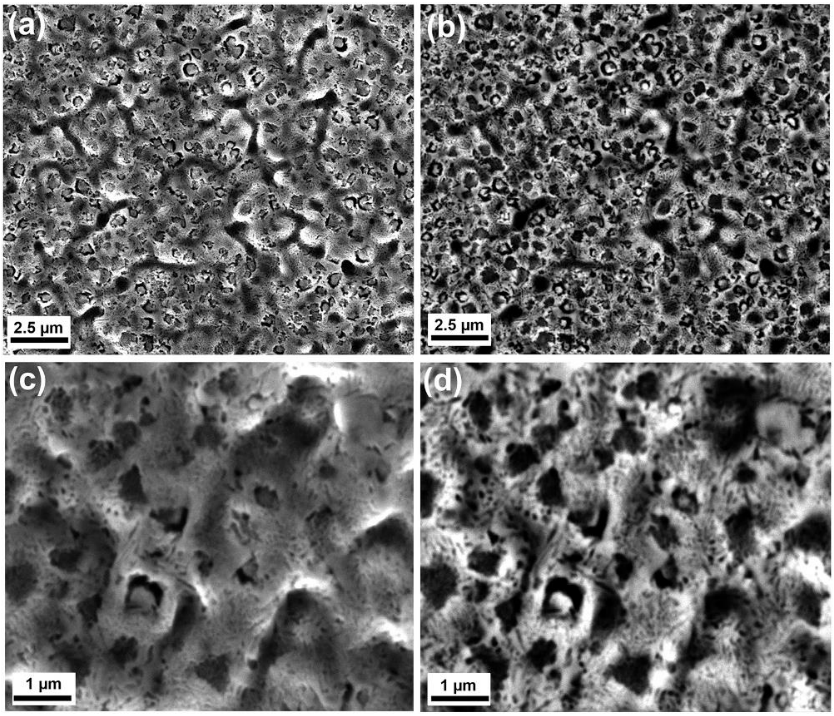

**Fig. 3.** Top surface view of NPG_5min; a) and c) SEM-SE images, b) and d) BSE images.

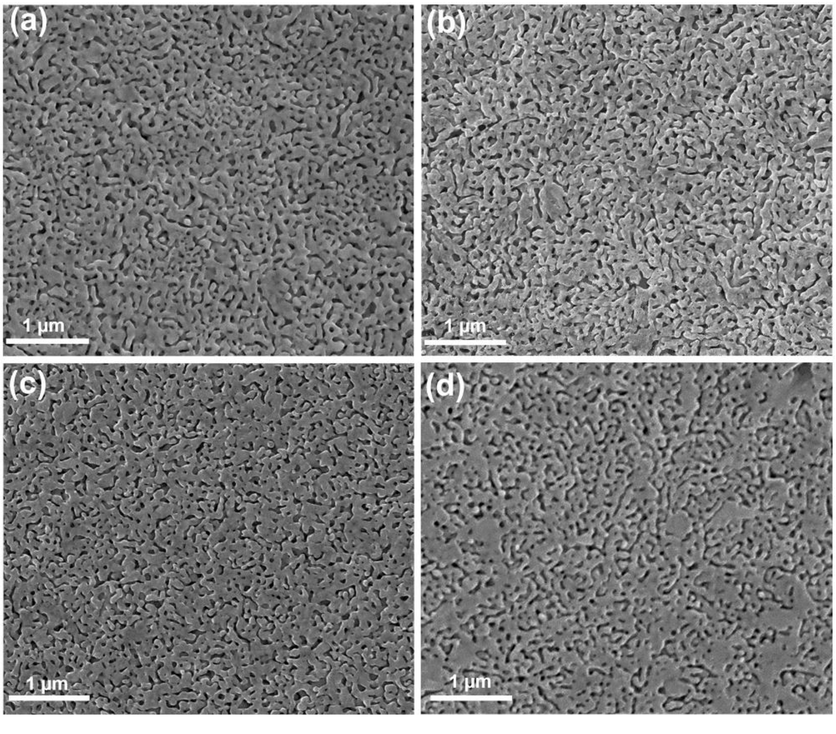

**Fig. 4.** SEM-SE images of (a) NPG_2h; (b) NPG_4h; (c) NPG_6h; and (d) NPG_8h.

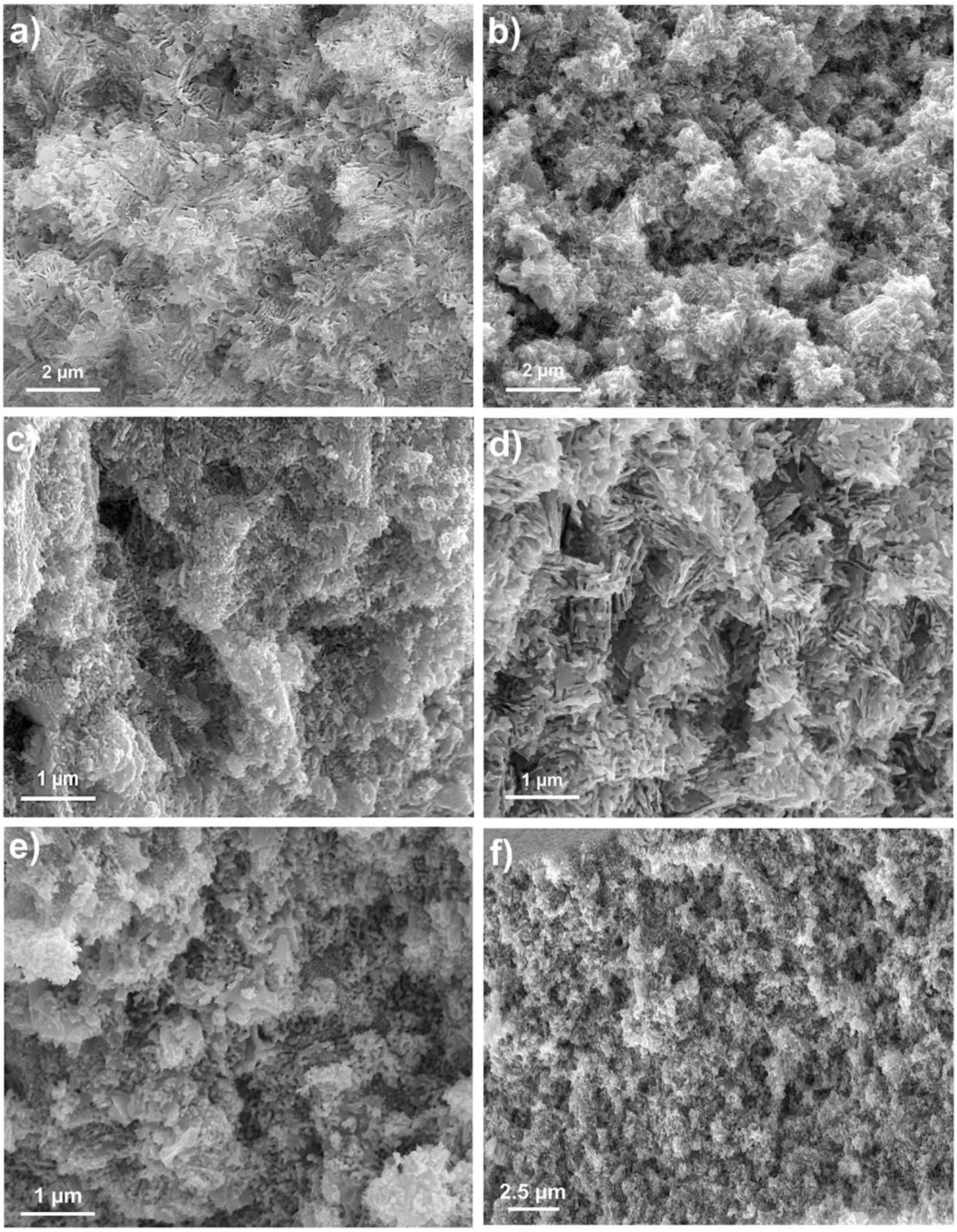

**Fig. 5.** The SEM-SE images of the cross sections of (a) NPG_1min, (b) NPG_5min, (c) NPG_10min, (d) NPG_30min, (e) NPG_1h and (f) NPG_8h.

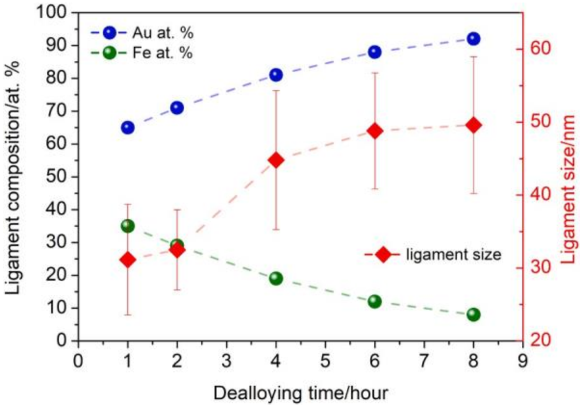

**Fig. 6.** Ligament composition and ligament size as a function of the dealloying time

## 3.3. Structural analyses and mechanism of dealloying

Rietveld analyses of XRD patterns at different etching times was helpful to clarify the evolution of phases and together with micro- structural and morphological characterization has led to unveil the mechanism of dealloying in $Au_{33}Fe_{67}$ crystalline metastable precursor. The refining was conducted by modelling the patterns with the four phases that appear progressively as a function of the time: two fcc (Au) solid solutions, respectively named fcc (Au) and fcc (Au)#2 with different iron amount, a bcc α (Fe) solid solution and fcc pure Au constituted by almost pure gold. The lattice parameter of the above- mentioned phases was reported for shorter durations of dealloying in Fig. 7(a) and for longer times in Fig. 7(b). Since the bcc α (Fe) solid solution is rapidly dissolved after one minute of dealloying from the sample's surface, solely the lattice parameter of the ICDD Au reference was considered for comparison. The error bar was measured as the variation of the lattice parameter due to a z-displacement equal to the thickness of the samples itself. The lattice parameter of fcc (Au) and fcc (Au)#2, within the error bar, does not change significantly during the dealloying process; at the same time the fcc pure (Au) displays a lattice parameter compatible to that of the Au reference pattern 03–065–8601. The fraction of phases in weight percent is reported in pie charts within the corresponding microstructure image as a function of dealloying time in the scheme of Fig. 8. As already mentioned the as- quenched ribbon contains three phases, fcc (Au), fcc (Au)#2, and bcc α(Fe); since fcc (Au)#2 is very limited in amount and displays the same behaviour of the main solid solution, the description of the mechanism will consider the fcc (Au) phase as comprehensive of both phases. As a consequence, the as-quenched ribbon is described with the fcc (Au) and bcc α(Fe) phases, whose weight fraction is 78.2 % and 21.8 % respectively. After one minute of dealloying, the bcc α(Fe) completely disappears due to galvanic effect from the surface and, at this stage, the system is composed solely of the fcc (Au).

As the dealloying process continues, the removal of the Fe atoms from the solid solution and the surface diffusion of Au ad-atoms lead to the growth of a fcc pure Au phase, whose fraction increases progressively as a function of time. After eight hours of dealloying only the fcc pure Au and fcc (Au) phases remain with a weight fraction of 60 % and 40 % respectively. Considering that the dealloying proceeds from the surface to the bulk of the ribbon and due to the limited penetration depth of the XRD technique, this dealloying mechanism describes the changes acting on the surface in contact with the electrolyte. Then, the inner portion of the sample that contacts the electrolyte will experience the same mechanism when the first layer is dealloyed.

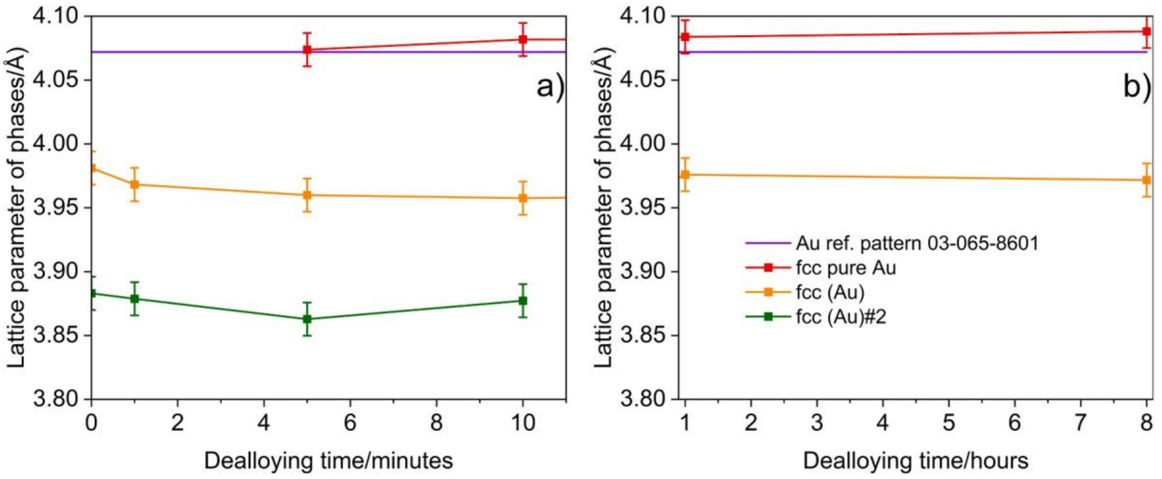

**Fig. 7.** Lattice parameter of phases as a function of dealloying time; a) short durations and b) longer durations.

**Fig. 8.** Scheme of the dealloying mechanism as a function of time in 1 M HNO$_3$. Pie charts represent the weight fraction of phases at different stages as evaluated from the Rietveld refinements of the diffraction patterns.

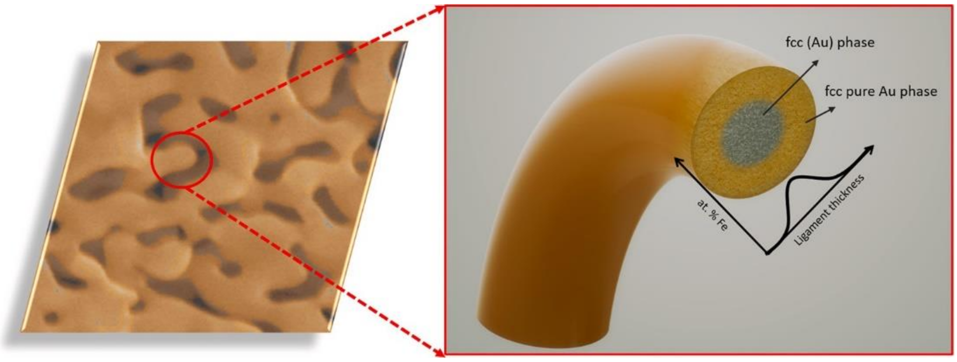

**Fig. 9.** Scheme of the compositional gradient inside a ligament due to the dealloying mechanism.

As a result of this dealloying mechanism, each ligament of the nanoporous structure experiences a gradient of composition along its cross section. As represented in Fig. 9, the inner core of each ligament is made up of the pristine fcc (Au) solid solution while the external part is constituted by the fcc pure Au phase that increases in weight fraction due to the aggregation by surface diffusion of Au ad-atoms freed from the other phases. The external pure Au layer passivates the surface, making the inner layer unavailable to the electrolyte. All these considerations are related to the information of the XRD on the sample surface. It can be expected that a limited amount of bcc α(Fe) phase is still pre- sent in the inner core of the ribbon, being prevented from dissolution owing to the presence of Au rich phase that passivates the region.

### 3.4. Magnetic characterization

Room-temperature hysteresis loops of the as-quenched Au33Fe67 ribbon and the NPG samples are shown in Fig. 10 (a). The magnetic moment is normalized to the sample mass to improve the comparison. The magnetization reversal process of the precursor ribbon is characterized by a hysteretic behavior with coercive field (Hc) and magnetization remanence (Mr) values of about 93 Oe and 22 emu/g, respectively. The saturation magnetization (Ms), achieved with a slow approach by increasing the magnetic field, is about 80 emu/g; this value is fully compatible with the ribbon microstructure observed by structural characterizations. In fact, it results from a balance between the high saturation magnetization proper of the bcc α(Fe) grains and the low saturation magnetization of the fcc (Au) solid solution [27].

In the NPG_1min sample, the M(H) curve maintains similar hysteretic properties. However, the saturation magnetization drops to 31 emu/g. The halving of the Ms value is closely related to the substantial and rapid dissolution of the bcc α(Fe) phase present on the ribbon surface, as revealed by the XRD spectra in Fig.

2(b).

By increasing the chemical dealloying time to 30 minutes, the Ms value progressively decreases to 20 emu/g with a lower slope compared to the first minute of treatment, see Fig. 10 (b), suggesting that the rate of bcc α(Fe) dissolution progressively slows down during the chemical attack infiltrates the ribbon and the ligaments are formed.

The further increase of the dealloying time from 30 minutes to 8 hours does not affect the magnetic properties. In fact, the shape of the hysteresis curves and the saturation magnetization value remain substantially unaltered within the measurement uncertainty. This result indicates that part of the bcc α(Fe) is still present in the inner part of the ribbon not reached by the electrolyte.

Structural and magnetic characterization agree in describing the dealloying mechanism of this metastable $Au_{33}Fe_{67}$ precursor except for the presence of the bcc α(Fe) phase that is still observed in magnetic measurements of samples dealloyed for longer durations but not in their corresponding XRD patterns. This seems reasonable considering that the magnetic characterization is a bulk technique, exploring the whole thickness of the sample, while the XRD measurements are limited to the surface; indeed, the X-rays penetration depth depends both on the experimental setup (i.e., intensity of the incident beam and angle), and largely on the density and linear absorption coefficient of the sample. The magnetic contribution of the bcc α(Fe) phase is still evident but reduced in magnetic measurements of samples after long dealloying durations.

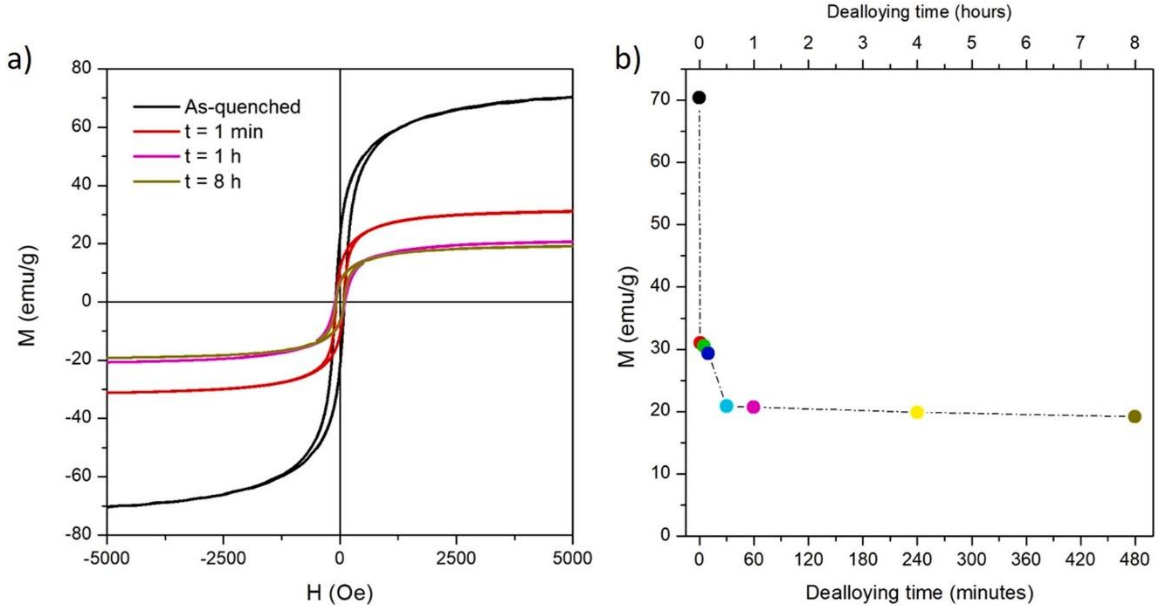

**Fig. 10.** a) Room-temperature hysteresis loops of as-quenched $Au_{33}Fe_{67}$ ribbon and NPG samples treated for selected dealloying time; b) Evolution of saturation magnetization ($M_s$) as a function of dealloying time.

## 4. Conclusion

Nanoporous Gold has been successfully produced by chemical dealloying in 1 M $HNO_3$ at 70 ◦C using as precursor a metastable supersaturated solid solution of $Au_{33}Fe_{67}$ obtained by melt-spinning techniques.

The obtained NPG is homogeneous with tunable ligament size and shape, easy-to-handle and free-standing. From the study of samples dealloyed for different times, it was possible to propose a mechanism of dealloying that starts with the dissolution, due to galvanic effects, of the bcc α(Fe) phase, followed by a progressive dissolution of Fe atoms from the fcc (Au) phase, with the creation of a passive layer on the ligaments formed of almost pure Au crystals. The results from magnetic investigations confirmed the interpretation of the dealloying mechanism made on the basis of the microstructural and structural analysis of the samples. Few trends are noticeable, i.e., with the increase in the dealloying time, there is an increase in - (i) the atomic percentage of Au; (ii) the size of the ligaments, and; (iii) the homogeneity of the surface morphology.

Combining structural and microstructural analysis with magnetic characterization has resulted in a multidisciplinary approach to the study of NPG, leading in the discovery of the mechanism of dealloying. Authors believe that this piece of science will contribute, as first, to extend the knowledge of dealloying of a Fe-rich biphasic metastable supersaturated Au-Fe solid solution. Secondly, it will positively impact the production of NPG by employing a fast, simple, and sustainable synthesis procedure combined with a cost-effective starting material, thus contributing towards the development of nanoporous materials for cutting-edge technologies.

**Funding**

This research was funded by Compagnia di San Paolo Bando ex-post 2020 WeSensBio 21/12/2021.

**CRediT authorship contribution statement**

Paola Rizzi: Writing – review & editing, Supervision, Resources, Investigation, Funding acquisition, Formal analysis, Data curation, Conceptualization. Deepti Raj: Writing – original draft, Visualization, Methodology. Federica Celegato: Methodology, Investigation, Data curation. Gianluca Fiore: Methodology, Investigation, Data curation. Gabriele Barrera: Writing – review & editing, Writing – original draft, Validation, Methodology, Investigation, Data curation, Conceptualization. Marco Coïsson: Methodology, Investigation, Formal analysis. Paola Tiberto: Writing – review & editing, Supervision, Investigation, Formal analysis, Data curation. Federico Scaglione: Writing – review & editing, Writing – original draft, Validation, Methodology, Investigation, Data curation, Conceptualization.

**Declaration of Competing Interest**

The authors declare the following financial interests/personal relationships which may be considered as potential competing interests: Prof. Paola Rizzi reports financial support was provided by Compagnia di San Paolo. If there are other authors, they declare that they have no known competing financial interests or personal relationships that could have appeared to influence the work reported in this paper.

**Data availability**

Data will be made available on request.

**Acknowledgements**

Acquisition of the SEM images has been performed thanks to NanoFacility Piemonte, INRIM. Authors acknowledge support from the Project CH4.0 under the MUR program “Dipartimenti di Eccellenza 2023–2027” (CUP: D13C22003520001).

## References

[1] J.K. Bhattarai, D. Neupane, B. Nepal, V. Mikhaylov, A.V. Demchenko, K.J. Stine, Structure and applications of gold in nanoporous form, Noble Precious Met. Prop. Nanoscale Eff. Appl. (2018), https://doi.org/10.5772/intechopen.71439.

[2] E. Vassileva, L. Mihaylov, L. Lyubenova, T. Spassov, F. Scaglione, P. Rizzi, Porous metallic structures by dealloying amorphous alloys, J. Alloy. Compd. 969 (2023) 172417, https://doi.org/10.1016/j.jallcom.2023.172417.

[3] E.M. Paschalidou, F. Scaglione, A. Gebert, S. Oswald, P. Rizzi, L. Battezzati, Partially and fully de-alloyed glassy ribbons based on Au: application in methanol electro-oxidation studies, J. Alloy. Compd. 667 (2016), https://doi.org/10.1016/j.jallcom.2016.01.181.

[4] F. Scaglione, E.M. Paschalidou, P. Rizzi, S. Bordiga, L. Battezzati, Nanoporous gold obtained from a metallic glass precursor used as substrate for surface-enhanced Raman scattering, Philos. Mag. Lett. 95 (2015) 474–482, https://doi.org/10.1080/ 09500839.2015.1093665.

[5] Y. Xue, F. Scaglione, P. Rizzi, L. Battezzati, P. Denis, H.-J. Fecht, Electrodeposited platinum on de-alloyed nanoporous gold with enhanced electro-catalytic performance, Appl. Surf. Sci. 476 (2019), https://doi.org/10.1016/j.apsusc.2019.01.099.

[6] F. Scaglione, Y. Xue, F. Celegato, P. Rizzi, L. Battezzati, Amorphous molybdenum sulphide @ nanoporous gold as catalyst for hydrogen evolution reaction in acidic environment, J. Mater. Sci. (2018), https://doi.org/10.1007/s10853-018-2490-2.

[7] S.H. Kim, Nanoporous gold: Preparation and applications to catalysis and sensors, Curr. Appl. Phys. 18 (2018) 810–818, https://doi.org/10.1016/j.cap.2018.03.021.

[8] I. McCue, E. Benn, B. Gaskey, J. Erlebacher, Dealloying and dealloyed materials, Annu. Rev. Mater. Res. 46 (2016) 263–286, https://doi.org/10.1146/annurevmatsci-070115-031739.

[9] J. Erlebacher, M.J. Aziz, a, N. Karma, K. Dimitrov, Sieradzki, Evolution of nanoporosity in dealloying, Nature 410 (2001) 450–453, https://doi.org/10.1038/35068529.

[10] J. Erlebacher, An atomistic description of dealloying, J. Electrochem. Soc. 151(2004) C614, https://doi.org/10.1149/1.1784820.

[11] J. Erlebacher, K. Sieradzki, Pattern formation during dealloying, Scr. Mater. 49(2003) 991–996, https://doi.org/10.1016/S1359-6462(03)00471-8.

[12] Z. He, Y. Huang, F. He, Preparation of nanoporous molybdenum film by dealloying an immiscible Mo–Zn system for hydrogen evolution reaction, RSC Adv. 6 (2016)15390–15393, https://doi.org/10.1039/C5RA24426A.

[13] X. Li, Q. Chen, I. McCue, J. Snyder, P. Crozier, J. Erlebacher, K. Sieradzki, Dealloying of noble-metal alloy nanoparticles, Nano Lett. 14 (2014) 2569–2577, https://doi.org/10.1021/nl500377g.

[14] The Materials Information Society, Alloy Phase Diagrams Provisional, Bull. Alloy Phase Diagrams. 3 (1982) 376–402. doi:10.1007/BF02869318.

[15] D.T.L. Alexander, D. Forrer, E. Rossi, E. Lidorikis, S. Agnoli, G.D. Bernasconi, J. Butet, O.J.F. Martin, V. Amendola, Electronic structure-dependent surface plasmon resonance in single Au–Fe nanoalloys, Nano Lett. 19 (2019) 5754–5761, https://doi.org/10.1021/acs.nanolett.9b02396.

[16] E. Bosco, P. Rizzi, M. Baricco, Phase transformations in Au-Fe melt spun alloys, Mater. Sci. Eng. A 375–377 (2004) 468–472, https://doi.org/10.1016/j.msea.2003.10.048.

[17] E. Bosco, P. Rizzi, M. Baricco, Rapid solidification of immiscible alloys, J. Magn. Magn. Mater. 262 (2003) 64–68, https://doi.org/10.1016/S0304-8853(03)00020-9.

[18] D. Raj, M. Palumbo, G. Fiore, F. Celegato, F. Scaglione, P. Rizzi, Sustainable nanoporous gold with excellent SERS performances, Mater. Chem. Phys. 293(2023) 126883, https://doi.org/10.1016/j.matchemphys.2022.126883.

[19] The L.O.N.D.O.N. METAL EXCHANGE The world centre for industrial metals trading, (n.d.). 〈https://www.lme.com/〉.

[20] E. Commission, I. Directorate-General for Internal Market Entrepreneurship and SMEs, G. Blengini, C. El Latunussa, U. Eynard, C. Torres De Matos, D. Wittmer, K. Georgitzikis, C. Pavel, S. Carrara, L. Mancini, M. Unguru, D. Blagoeva, F. Mathieux, D. Pennington, Study on the EU's list of critical raw materials (2020) – Final report, Publications Office of the European Union, 2020. doi:doi/10.2873/11619.

[21] D. Raj, F. Scaglione, G. Fiore, F. Celegato, P. Rizzi, Nanostructured molybdenum oxides from aluminium-based intermetallic compound: synthesis and application in hydrogen evolution reaction, Nanomaterials 11 (2021), https://doi.org/10.3390/nano11051313.

[22] Z. Zhang, Y. Wang, Y. Wang, X. Wang, Z. Qi, H. Ji, C. Zhao, Formation of ultrafine nanoporous gold related to surface diffusion of gold adatoms during dealloying of Al2Au in an alkaline solution, Scr. Mater. 62 (2010) 137–140, https://doi.org/10.1016/j.scriptamat.2009.10.018.

[23] S. Van Petegem, S. Brandstetter, A.M. Hodge, B.S. El-Dasher, J. Biener, B. Schmitt, C. Borca, H. Van Swygenhoven, On the microstructure of nanoporous gold: an Xray diffraction study, Nano Lett. 9 (2009) 1158–1163, https://doi.org/10.1021/nl803799q.

[24] Y. Xue, S. Wang, P. Shi, Y. Huang, F. Scaglione, P. Rizzi, L. Battezzati, P. Denis, H. J. Fecht, Nanoporous gold chemically de-alloyed from Au-based amorphous thin film for electrochemical nonenzymatic H 2 O 2 sensing, Chem. Phys. Lett. 723(2019) 22–27, https://doi.org/10.1016/j.cplett.2019.03.024.

[25] W.H. Lutterotti SML, MAUD (Material Analysis Using Diffraction) is released under free license of the authors., (n.d.).

[26] P.S.M. Kumar, T. Sivakumar, T. Fujita, R. Jayavel, H. Abe, Synthesis of metastable Au-Fe alloy using ordered nanoporous silica as a hard template, Metals 8 (2018) 1–7, https://doi.org/10.3390/met8010017.

[27] P. Allia, M. Coisson, V. Selvaggini, P. Tiberto, F. Vinai, Observation of isotropic giant magnetoresistance in paramagnetic Au80 Fe20, Phys. Rev. B Condens. Matter Mater. Phys. 63 (2001) 18–21, https://doi.org/10.1103/PhysRevB.63.180404.